

Accepted Manuscript

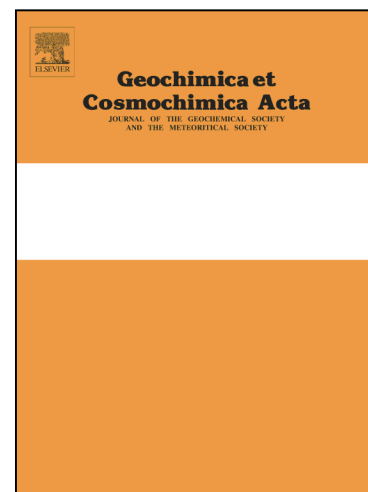
Quantification of non-ideal effects on diagenetic processes along extreme salinity gradients at the Mercator mud volcano in the Gulf of Cadiz

Laura Haffert, Matthias Haeckel

PII: S0016-7037(18)30574-X
DOI: <https://doi.org/10.1016/j.gca.2018.09.038>
Reference: GCA 10961

To appear in: *Geochimica et Cosmochimica Acta*

Received Date: 25 August 2017
Accepted Date: 29 September 2018



Please cite this article as: Haffert, L., Haeckel, M., Quantification of non-ideal effects on diagenetic processes along extreme salinity gradients at the Mercator mud volcano in the Gulf of Cadiz, *Geochimica et Cosmochimica Acta* (2018), doi: <https://doi.org/10.1016/j.gca.2018.09.038>

This is a PDF file of an unedited manuscript that has been accepted for publication. As a service to our customers we are providing this early version of the manuscript. The manuscript will undergo copyediting, typesetting, and review of the resulting proof before it is published in its final form. Please note that during the production process errors may be discovered which could affect the content, and all legal disclaimers that apply to the journal pertain.

Quantification of non-ideal effects on diagenetic processes along extreme salinity gradients at the Mercator mud volcano in the Gulf of Cadiz

Laura Haffert¹ and Matthias Haeckel¹

¹ GEOMAR Helmholtz Centre for Ocean Research Kiel, Wischhofstrasse 1-3, 24148 Kiel, Germany

Abstract

We present a transport-reaction model (TRACTION) specifically designed to account for non-ideal transport effects in the presence of thermodynamic (e.g. salinity or temperature) gradients. The model relies on the most fundamental concept of solute diffusion, which states that the chemical potential gradient (Maxwell's model) rather than the concentration gradient (Fick's law) is the driving force for diffusion. In turn, this requires accounting for species interactions by applying Pitzer's method to derive species chemical potentials and Onsager coefficients instead of using the classical diffusion coefficients. Electrical imbalances arising from varying diffusive fluxes in multicomponent systems, like seawater, are avoided by applying an electrostatic gradient as an additional transport contribution. We apply the model to pore water data derived from the seawater mixing zone at the submarine Mercator mud volcano in the Gulf of Cadiz. Two features are particularly striking at this site: (i) Ascending halite-saturated fluids create strong salinity (NaCl) gradients in the seawater mixing zone that result in marked chemical activity, and thus chemical potential gradients. The model predicts strong transport-driven deviations from the mixing profile derived from the commonly used Fick's diffusion model, and is capable of matching well with the profile shapes observed in the pore water concentration data. Even better agreement to the observed data is achieved when ion pairs are transported separately. (ii) The formation of authigenic gypsum (several wt%) occurs in the surface sediments, which is typically restricted to evaporitic surface processes. Very little is known about the gypsum paragenesis in the subseafloor and we first present possible controls on gypsum solubility, such as pressure, temperature, and salinity (pTS), as well as the common ion and ion pairing effects. Due to leaching of deep diapiric salt, rising fluids of the MMV are saturated with respect to gypsum (as well as celestite and barite). Several processes that could drive these fluids towards gypsum supersaturation and hence precipitation were postulated and numerically quantified. In line with the varied morphology of the observed gypsum crystals, gypsum paragenesis at the MMV is likely a combination of two temperature-related processes. Gypsum solubility increases with increasing temperature, especially in strong electrolyte solutions and the first mechanism involves the cooling of saturated fluids along the geothermal gradient during their ascent. Secondly, local temperature changes, i.e. cooling during the transition from MMV activity towards dormancy results in the cyclic build-up of gypsum. The model showed that the interpretation of field data can be majorly misguided when ignoring non-ideal effects in extreme diagenetic settings. While at first glance the pore water profiles at the Mercator mud volcano would indicate strong reactive influences in the seawater mixing zone, our model shows that the observed species distributions are in fact primarily transport-controlled. The model results for SO_4 are particularly intriguing, as SO_4 is shown to diffuse into the sediment along its increasing (!) concentration gradient. Also, a pronounced gypsum

saturation peak can be observed in the seawater mixing zone. This peak is not related to the dissolution of gypsum but is simply a result of the non-ideal transport forces acting on the activity profile of SO_4 and Ca profiles.

Introduction

Geochemical transport-reaction models often play an essential role in the interpretation of field data in terms of coupled physical, chemical and biological processes in the Earth system. One of their most important applications is the quantitative analysis of solute porewater-depth profiles. These models have the capability to confirm whether or not certain physical or chemical changes or reactions are occurring in the sedimentary column and provide us with a means to evaluate the overall chemical exchange (fluxes) between two important Earth reservoirs. Unfortunately, accurate numerical modelling in thermodynamically heterogeneous settings remains a challenge because most geochemical reactive transport models ignore solute coupling and activity effects. This is a simplification that is justified for relatively dilute compositions and in the absence of strong thermodynamic gradients.

Here we present a model that accounts for non-ideal effects on solute transport and reaction processes in extreme diagenetic settings. In this context, the classical marine transport-reaction model (e.g. Berner, 1980; Boudreau, 1996; Haeckel et al., 2001) was substantially extended to account for the complex thermodynamic forces driving the diffusive flux of the solutes Na, K, Ca, Mg, Li, Ba, Sr, Cl, SO_4 . We apply Onsager diffusion coefficients derived by Felmy and Weare (1991) for concentrated multicomponent solutions to account for short-range ionic interactions. The Pitzer method (e.g. Pitzer, 1973) is employed to compute changes in species activities, which are used to derive solute chemical potentials required for the diffusive model and to accurately describe equilibrium reactions, such as ion pairing and mineral solubilities. The resulting combination of transport-reaction framework and Pitzer method is a unique and powerful simulation tool (TRACTION) that can be applied to a wide variety of heterogeneous natural settings, including concentrated multicomponent solutions in high temperature, high-pressure, and/or high-salinity environments.

We demonstrate the predictive capability of our model by investigating unusual porewater profiles at the sediment-seawater interface of the Mercator mud volcano (MMV) in the Gulf of Cadiz (Figure 1). The MMV does not expel any mud at present (Haffert et al., 2013); it is however active as a weak cold vent with fluid flow velocities of a few centimetres per year. These fluids have experienced a genesis similar to those of other mud volcanoes in the Gulf of Cadiz located above deeply rooted fault systems. These processes include clay mineral dewatering, thermogenic degradation of organic matter and high-temperature leaching of terrigenous sediments or continental crust (Haffert et al., 2013; Hensen et al., 2007; Scholz et al., 2009). The MMV is a rare case where interaction with a diapir at depth (ca 500 m.b.s.f. and primarily consisting of Triassic evaporates such as halite, gypsum, anhydrite, sylvite and carnallite) significantly alters the diagenetic signal of the pore fluids by increasing the salinity to halite saturation through dissolution. Furthermore, while shallow porewater profiles of the mud volcanoes in the Gulf of Cadiz are generally dominated by anaerobic oxidation of methane (AOM) and associated carbonate precipitation (Hensen et al., 2007; Niemann et al., 2006; Scholz et al., 2009; Sommer et al., 2009), the shallow diagenesis at the MMV is instead dominated by transport phenomena arising from the strong salinity gradient in the seawater-sediment mixing zone (Haffert et al., 2013). The presence of authigenic gypsum in the shallow sediments also sets this mud volcano apart from others because supersaturation of fluids with respect to gypsum is typically restricted to

evaporitic processes. Only few reports exist on non-evaporitic gypsum in marine sediments and these offer varying hypotheses regarding its origin. Explanations are based on a range of deciding factors, such as the alteration of volcanogenic material or basaltic basement (Hoareau et al., 2011), changes from anoxic to oxic conditions in the presence of pyrite and carbonates (Bain, 1990; Pirlet et al., 2010; Siesser and Rogers, 1976) and gas hydrate formation (Wang et al., 2004). None of the above processes are relevant to the MMV setting demanding a new concept for the precipitation of authigenic gypsum and anhydrite.

Methods

Model equations

The classical approach used in early diagenetic modelling consists of partial differential equations representing the diffusive (J_i^{diff}) and advective (J_i^{adv}) fluxes coupled to a reaction term, as formulated by Berner (1980):

$$\frac{\partial \phi C_i}{\partial t} = - \frac{\partial}{\partial x} (\phi J_i^{diff} + \phi J_i^{adv}) - \phi R(C_i) \quad (1)$$

where t and x represent time and the depth under the seafloor, respectively. C_i is the molar species concentration of ion i , which is converted via the porosity ϕ to a bulk sediment concentration, and $R(C_i)$ represents all source and sink reaction rates affecting C_i .

The expression for the diffusive flux is often based on the simplified Fick's first law (Fick, 1855), subsequently referred to as the *Fickian model*, and assumes that the transport of porewater constituents occurs independently, i.e. the motion of one solute species will not influence the transport of another solute:

$$J_i^{diff} = - D_i \frac{\partial C_i}{\partial x} \quad (2)$$

where D_i is the molecular diffusion coefficient.

The upward advective flux is expressed as

$$J_i^{adv} = u C_i \quad (3)$$

where u is the fluid velocity.

Outside the range of dilute solutions (ionic strengths of $I > 0.1-0.3$), irreversible thermodynamics shows that the diffusive flux in multicomponent systems is governed by the magnitude of the applied thermodynamic force rather than the concentration gradient (Onsager, 1931; Onsager and Fuoss, 1932):

$$J_i^{diff} = \sum_{j=1}^N l_{ij} X_j \quad (4)$$

where j , like i , represents an ion species, X_j describes the thermodynamic force acting on ion j and the (solvent-fixed) Onsager phenomenological coefficient l_{ij} , in turn, accounts for the effectiveness to comply with the thermodynamic force, i.e. short-range ionic interaction. Incorporating off-diagonal Onsager coefficients (i.e. l_{ij} with $i \neq j$) accounts for the flux of ion i resulting from the forces acting on ion j .

In isothermal systems and in the absence of external gravitational or magnetic forces, the thermodynamic force (X_j) equates to the electrochemical potential (X_j^E):

$$X_j^E = - \left(\frac{\partial \mu_j}{\partial x} + z_j F \frac{\partial \varphi^E}{\partial x} \right) \quad (5)$$

Where z_j is the charge of ion j , F is the Faraday's constant, and $\frac{\partial \mu_j}{\partial x}$ and $\frac{\partial \varphi^E}{\partial x}$ represent the chemical potential and electrostatic spatial gradient, respectively. The latter is expressed as (Lasaga, 1979):

$$\frac{\partial \varphi^E}{\partial x} = - \frac{\sum_{m=1}^N \sum_{n=1}^N z_m l_{mn} \frac{\partial \mu_n}{\partial x}}{F \sum_{m=1}^N \sum_{n=1}^N z_m z_n l_{mn}} \quad (6)$$

and is derived from electroneutrality constraints requiring that (i) the total charge is zero throughout the solution ($\sum_{i=1}^N z_i C_i = 0$) and that (ii) no electrical current should run through the solution ($\sum_{i=1}^N z_i J_i = 0$). The label m and , just like i and j represent ion species in solution.

Inserting the above expressions into Equation (4) and implementing the relationship that the chemical potential (μ_i) is related to the standard chemical potential (μ_o) and activity (a_i) by $\mu_i = \mu_o + RT \ln a_i$, produces the equation for the diffusive flux that is used in the presented model, hereafter referred to as the *Onsager model*:

$$J_i^{diff} = RT \sum_{j=1}^N l_{ij} \left(- \frac{1}{a_j} \frac{\partial a_j}{\partial x} + z_j \frac{\sum_{m=1}^N \sum_{n=1}^N z_m l_{mn} \frac{1}{a_n} \frac{\partial a_n}{\partial x}}{\sum_{m=1}^N \sum_{n=1}^N z_m z_n l_{mn}} \right) \quad (7)$$

Where R is the universal gas constant, T is the absolute temperature and a is the species activity. The activity is defined as the product of the activity coefficient (γ_i) and the molal concentration ($a_i = \gamma_i m_i$).

Transport models usually transport molar concentration units, which greatly complicates the use of Onsager phenomenological coefficients in these models. For ease of use, Equation (7) can be further optimised for the direct use in a Fickian transport model by deriving an expression for the multicomponent diffusion coefficient D_{ik} as outlined by Felmy and Weare (1991):

$$J_i^{diff} = - \sum_{j=1}^N D_{ik} \frac{\partial C_i}{\partial x} \quad (8)$$

In infinitely dilute solutions or in the absence of suitable Onsager phenomenological coefficients, off-diagonal coefficients approach zero ($l_{ij}^o = 0$) and Equation (4) simplifies to

$$J_i^{diff} = l_{ii} X_i \quad (9)$$

In this case, the Onsager phenomenological coefficients can be related to the ideal (*Fickian*) diffusion coefficient (D_i^o):

$$l_{ii}^o = \frac{D_i^o C_i}{RT} \quad (10)$$

And the flux equation simplifies to

$$J_i^{diff} = -\frac{D_i^0 C_i \partial a_i}{a_i \partial x} + D_i^0 C_i z_i \frac{\sum_{k=1}^N z_k D_k^0 C_k \frac{1}{a_k} \frac{\partial a_k}{\partial x}}{\sum_{k=1}^N z_k^2 D_k^0 C_k} \quad (11)$$

This study relies greatly on the correct calculation of species activities to determine transport and equilibrium properties of a solution. While in dilute solutions (ionic strength of up to 0.1 mol L⁻¹) an extended version of the Debye-Hückel equation is commonly applied to determine the activity coefficients (Debye and Hückel, 1923), in more concentrated solutions short-range species interactions play an increasingly important role and more comprehensive methods should be applied. This work follows the example of Pitzer (1973) Pitzer (1973), Pitzer and Mayorga (1973a,b) and Pitzer and Kim (1974), who re-examined the statistical mechanics of electrolytes in water and derived a semi-empirical approach. The Pitzer model is applicable over an exceptional wide pTS range and can easily accommodate the conditions found at the MMV. Over the years slightly different adaptations of the Pitzer equation has been published, the equations used in the presented models are outlined in the Supplementary Material (S3).

Equilibrium calculations that can establish the saturation state or solubility of the sulfate minerals gypsum, anhydrite, barite and celestite can generally be approached in two ways. In well-studied systems like pure water or standard seawater the stoichiometric equilibrium constant K^* can be directly used in conjunction with the relevant species concentrations:

$$K^* = \frac{[C]^c [D]^d}{[A]^a [B]^b} \quad (12)$$

where $[C]$, $[D]$ and $[A]$, $[B]$ are the concentrations of the reaction products and educts, respectively, and the exponents a , b , c , d represent their stoichiometric factors. While stoichiometric equilibrium constants are very practical to use, they are limited to the pTS conditions they were derived for. A more general approach is offered by the use of the thermodynamic equilibrium constants (K), which defines the chemical equilibrium in terms of species activities (a_i) rather than concentrations:

$$K = \frac{a_C^c a_D^d}{a_A^a a_B^b} \quad (13)$$

The saturation state (Ω) of a mineral can be deduced by comparing the actual ion activity product (IAP) in the solution with the thermodynamic equilibrium constant:

$$\Omega = IAP/K \quad (14)$$

If the saturation state takes on a value larger or smaller than one, the solution is supersaturated or undersaturated, respectively.

Solubility calculations depend strongly on the complexity of the ambient solution. When dissolved in pure water, for example, the solute species are present at the same stoichiometric ratio as in the mineral. Based on the appropriate mass balance expression the solubility s can be derived solely from thermodynamic parameters (here shown for gypsum):

$$s_{gy} = \sqrt{\frac{K_{gy}}{\gamma_{\pm}^2 a_{H_2O}^2}} + \frac{K_{gy}}{a_{H_2O}^2 \gamma_{CaSO_4^{\circ}} K_{CaSO_4^{\circ}}} \quad (15)$$

where γ_{\pm} is the mean activity coefficient (when dissolved in pure water γ_{SO_4} equals γ_{Ca}). In multicomponent solutions, solubility calculations are being complicated by (1) different values for the activity coefficients, here γ_{SO_4} and γ_{Ca} , and (2) the potential non-stoichiometric distribution of the solutes in the presence of other ion pairs, e.g. HSO_4^- , or the common ion effect. The latter is defined as the changes that occur when an electrolyte is added to an existing solution that already contains one of the electrolyte ions, e.g. the adding of $CaCl_2$ or $NaSO_4$ to a solution containing $CaSO_4$.

Model specifications

All necessary parameters and constants used within the numerical transport-reaction model are given in Table 1 (transport) and Table 2 (reaction) as well as the figure caption of the respective simulation plot. Details of the coupling effects acting on each individual species are provided in Table 3. Whether or not a species is coupled to another species is decided mainly by data availability and some minor model simplifications (Supplementary Material S1 and S4). An example of the model code is available in the PANGAEA database (Haffert and Haeckel, 2018).

Constant concentrations of dissolved species were prescribed at the upper and lower boundary for all diagenetic models (Dirichlet boundary conditions) while the vertical distribution of solids was simulated by applying Dirichlet conditions only at the upper boundary and setting a no-gradient constraint at the lower boundary (Neumann conditions). Observed porewater data suggest that rising MMV fluids are saturated with respect to halite, gypsum, barite and celestite and the lower boundary conditions of the relevant solutes were set accordingly (Figure 2 and Haffert et al., 2013). Na and Cl boundary conditions were further constrained by the need to maintain electroneutrality.

Few authors have parameterized the calculation of Onsager phenomenological coefficients. Here, we follow the approach by Felmy and Weare (1991) who successfully described the diffusive flux in the multicomponent Na-K-Ca-Mg-Cl-SO₄-H₂O system at 25°C.

Since the original Pitzer formalism was first established (Pitzer, 1973), numerous Pitzer datasets have been published. For the purpose of this modelling work we have created a temperature flexible dataset (0-100 °C) mainly based on the work of Christov (2012), Christov and Moller (2004a, b) and Lassin et al. (2015). For the volumetric Pitzer dataset we relied on the data of Krumgalz et al. (2000; 1999). Details on the implementation and validation of the Onsager transport and Pitzer activity model are provided in the Supplementary Material (S1-S5).

In order to highlight specific transport effects on species distribution various *transport-only* models were constructed, which do not incorporate any diagenetic reactions (Table 4): (i) The *Onsager model* (Equation (7)) represents the most comprehensive transport model for extreme pTS settings. It uses Onsager phenomenological coefficients where appropriate and transports the most important sulfate ion pairs ($CaSO_4^{\circ}$, $MgSO_4^{\circ}$ and $NaSO_4^-$) as individual species. (ii) For comparison, a *total concentration model* was scripted that is identical to the Onsager model with the exception that it does not transport ion pairs as separate species. (iii) The error that is introduced by

simply using the concentration gradient as the driving force behind diffusion at the MMV is exposed by applying the *Fickian model* (Equation (2)), the most common diffusion model applied in diagenetic models.

The work on sulfate mineral paragenesis relies on a *transport-reaction model*, which uses the Onsager-transport model and includes reactive contributions of gypsum (dissolution and precipitation). This model is applied to quantify gypsum precipitation in the zone of gypsum supersaturation in the seawater mixing zone. Reaction kinetics for gypsum can be highly variable and, in addition to the saturation state, strongly depend on temperature and solution speciation (van Driesche et al., 2017). Thus, a wide range of values ($0.01 - 100 \text{ mmol L}^{-1} \text{ a}^{-1}$) are assumed for k_{gy} so as to cover all possible scenarios.

Gypsum precipitation related to the environmental changes of rising volcanic fluids are investigated by a simple box model which computes the decrease in gypsum solubility between the anhydrite/transition zone and the seafloor at various combinations of fluid velocities ($1 - 500 \text{ cm a}^{-1}$) and geothermal gradients ($30 - 25000 \text{ }^{\circ}\text{C km}^{-1}$). Kinetic constraints are assumed to be negligible due to the slow nature of this process, i.e. the travel from the diapir at 500 m depth to the surface is around 3000 years. In another box model, the build-up of gypsum as a result of repetitive cooling of saturated rising fluids was computed also based on the difference in gypsum solubility with varying temperatures.

Ion pairing – theoretical considerations

In addition to the coupling effects inherent to the transport model (i.e. via Onsager phenomenological coefficients, Pitzer activity coefficients and the electrostatic field), some species are reactively coupled through the formation of ion pairs. Ion pairs are formed through the association of oppositely charged ions (i.e. Marcus and Hefter, 2006) and in contrast to their influence on thermodynamic properties of seawater, which is nowadays well established (Felmy and Weare, 1986; Harvie et al., 1984; Millero and Schreiber, 1982), the role of ion pairing in transport-reaction simulations is still poorly defined. If a significant quantity of a solute is associated, migration of this species is at least in part carried out by its ion pairs. In fact, Katz and Ben-Yaakov (1980) and Lasaga (1981) suggested that the individual transport of ion pairs can result in a noticeable shift of the total concentration profile in the presence of a concentration gradient of one of the contributing ions ('hitchhiking effect'). More generally, these shifts can be expected in the presence of any sufficiently strong compositional gradients, because ion pairs have very different transport properties compared to the free species and potential coupling effects act very differently on them:

- (i) Compared to free solutes, the activity coefficients of the ion pairs are affected differently by changes in the solution's composition and their gradients are thus substantially different from free species. For example, the activity coefficient of SO_4 decreases downcore by 75% from 0.12 to 0.03 at the MMV, while the activity coefficient of the dominant NaSO_4^- ion pair (estimated from HSO_4^-) increases from 0.65 to 1.00 (Table 1) and the activity coefficient of neutral ion pairs is even less sensitive (here approximated by unity along the entire model domain).
- (ii) Electrostatic forces act very differently on the free species, which are more charged than their ion pairs. For example, neutral ion pairs like CaSO_4^0 and MgSO_4^0 are not affected by electrostatic forces at all, while the free divalent SO_4 is very strongly influenced by the electrostatic field.
- (iii) The diffusion coefficients of the associated species are usually greater than those of the free species (Table 1). This is generally attributed to the loss of hydration water upon ion pair formation, thus

lowering the effective cross section and related drag (Harned and Owen, 1958; Robinson and Stokes, 1959).

Another important and often overlooked consideration is the fact that the Pitzer-derived activity, in other words the effective concentration, has been corrected for non-ideal effects such as ion pairs. With the exception of CaSO_4° and HSO_4^- , the presence of ion pairs is resolved internally within the parameterisation of the Pitzer coefficients. As a consequence the activity coefficients for Ca and SO_4 can only be applied to the free concentrations, i.e. they do not include the CaSO_4° ion pair. Transport forces calculated based on these Pitzer-derived activity gradients, or more precisely chemical potential gradients, are valid only for the free species, i.e. they should only be applied to the profile of the free species. If the total concentration is transported instead (total concentration model, Table 4), it is assumed that the same forces that act on the free ions also act on the ion pairs, which can be an unacceptable assumption if a significant amount of a solute is transported by its ion pairs. In our simulations we transport the most abundant sulfate ion pairs separately (CaSO_4° , MgSO_4° and NaSO_4^-) assuming unity for the activity coefficient of the neutral species and estimating the NaSO_4^- activity coefficient from the HSO_4^- activity coefficient calculated with the Pitzer method. Interestingly, despite the constant activity coefficient assumed for neutral species, changes in the solution ionic strength still influence the species' chemical potential gradient via the molar/molal conversion factor ranging at the MMV from 1.01 at the seafloor to 1.13 at depth.

Modelling results

Transport-induced solute accumulation and depletion

Major solutes (Na, Ca, K, Mg, Li, Cl and SO_4) and species involved in the dominant SO_4 association reactions (Na, Sr and Ba) were simulated using the Onsager model (transport only, Table 4). Modelled profiles and the corresponding analytical porewater data from the MMV Bubble sites are compared in Figure 2a-i. In the upper 2 m of the seafloor, seawater mixes with volcanic fluids, which are saturated with respect to halite, gypsum, barite and celestite and are particularly enriched in Ca (> 80 mM), Li (> 3 mM) and Sr (> 0.8 mM) and depleted in SO_4 (<20 mM). The strong compositional changes are also reflected in a strong downcore increase in the solution density and decrease in the activity of water reaching asymptotic values below 3 m of up to 1.2 g/cm³ and 0.75, respectively (Figure 3). Within this mixing zone, most species display strong divergences from the typical mixing profile, including pronounced concentration peaks (SO_4 and Ba) or troughs (Mg, K). Excellent modelling fits could be achieved for Na, K, Mg and Cl. Slight discrepancies occur for SO_4 , Ca, Li, and Sr, whereas the Ba profile shows significant divergences. Ba tends to be present as the BaSO_4° ion pair in concentrated solutions (50% in 0.01 M sodium sulfate solutions, Monnin, 1999) and the misfit is likely related to the omission of this ion pair in the transport model due to a lack of available data.

For comparison, model results based on the Fickian model are also plotted in Figure 2a-i (grey line). The misfit of the Onsager model is generally much smaller than for the Fickian model. The largest improvement over the Fickian model is observable in the Mg and SO_4 profiles, where the strongest deviations from the simple mixing line occur in the analytical data.

With the help of the model, transport-only induced accumulation and depletion of species could directly be related to the different rates shaping the profile, which will be shown here for the example of SO_4 . Diffusion rates of SO_4 are driven by the decreasing profile of the excess chemical potential profile, demonstrating that seawater derived SO_4 diffuses into the sediment (Figure 4a), which is to be expected as the rising fluids are depleted with respect to SO_4 (Figure 2b). Thus, the chemical potential rather than the concentration profile is constrained by balanced steady state forces and the existence of the SO_4 peak is related to the fact that the SO_4 activity coefficient is dramatically reduced over the upper 100 cm from 0.12 to 0.04. With the activity coefficient being controlled by the overall solution composition, it is the SO_4 concentration that must compensate for this sudden change in the activity coefficient so as to maintain equilibrium for the chemical potential profile. This relationship is easily established when plotting the natural logarithm of the activity coefficient and the molal concentration, the sum of which represents the natural logarithm of the activity ($\ln a_{\text{SO}_4} = \ln \gamma_{\text{SO}_4} + \ln m_{\text{SO}_4}$), the main variable in the calculation of the excess chemical potential ($\mu_{ex} = RT \ln a_i$); the $\ln a_{\text{SO}_4}$ profile is representative of a typical mixing line whereas the $\ln \gamma_{\text{SO}_4}$ profile negatively imitates the strong spatial $\ln \gamma_{\text{SO}_4}$ gradient (Figure 4a,b).

While the strong spatial changes in the activity coefficients are the main reason behind the observed profile shapes, solute transport is also significantly affected by electrostatic effects. At the MMV, the electrical field (Figure 3c) generally induces downward diffusion of anions and vice versa for cations, with multivalent ions naturally being more strongly affected than univalent ions. The electrical field is mainly created by the strong NaCl gradient and its influence is generally strongest in the upper 100 cm where the spatial derivative of the electrostatic expression (Equation (5)) is most influential. In the case of SO_4 , the effect of the electrostatic field is simply observed as an enhancement of the SO_4 peak.

Incorporating the electrostatic effects into the simulations does not only improve modelled species profiles but plays an important role in maintaining electroneutrality within the modelled solution. Omitting these electrostatic effects (Fickian model) results in an extreme violation of the zero-charge law (electroneutrality) with up to 800 meq L^{-1} of charge ($\sum_{i=1}^N z_i C_i$) at around 100 cm depth at the Bubble site (Figure 3d). This would be equivalent to an addition of 800 mM Na to an uncharged solution and is clearly unacceptable as a valid modelling result.

Lastly it should be noted, that the fact that we can observe these transport processes in the upper metres of the seafloor is due to a balanced interplay of advection and diffusion. Advection pushes the transport phenomena within metres of the seafloor, but when advection is too strong, the effect is overridden: If the fluid velocity is too fast, the advective overriding of SO_4 accrual with SO_4 depleted fluids prevents the peak from forming. This can be observed at the Top site, (Figure 1) where fluid advection is relatively high ($u = 5 \text{ cm a}^{-1}$, Peclet number of 17) and the diffusion-driven SO_4 peak, for example, is reduced to a slight deviation from the ideal mixing line (Haffert et al., 2013). With the decreasing influence of advection, the diffusion-driven non-ideal redistribution of species becomes relatively more important and can be clearly discernible at the Bubble site ($u = 1.5 \text{ cm a}^{-1}$, Peclet number of 5). With the diminishing influence of advection, however, the non-ideal effects on species distribution becomes less apparent because the spatial salinity gradient ($\frac{\partial \sum C_i}{\partial x}$) and thus activity coefficient gradients ($\frac{\partial \gamma_i}{\partial x}$) are much weaker and the SO_4 peak, for example, would be much wider, observable only over a greater depth and likely overridden by diagenetic

processes such as AOM and organic matter degradation (e.g. West site, Figure 1, with $u = 0.1 \text{ cm a}^{-1}$ and a Peclet number of 0.3).

The prominence of the transport phenomena also affects the initial fitting of the advection velocity and has to be taken into account especially when advection rates are in the order of the diffusion rates, i.e. for Peclet numbers < 10 . At the Bubble site, the error arising from applying the Fickian rather than the Onsager model was found to exceed 50% in some cases, especially when fitting trace elements like Li (Supplementary Material S6).

Effect of ion pairing

Almost 50% of the SO_4 is present as one of its ion pairs at the seafloor, increasing to over 70% in the rising MMV fluids (Figure 4c). In fact, the diffusive input of free SO_4 into the sediment is entirely lost to ion pair formation (Figure 4g). As ion pairs are generally less affected by non-ideal effects (such as the strong decrease in the activity coefficient or electrostatic gradient), the overall transport fluxes of SO_4 are lowered when transporting ion pairs separately, as can be seen when combining and simplifying the rates of all SO_4 species (Figure 4f). As a result, the ion pair model predicts the characteristic SO_4 peak to be significantly less pronounced which improves the agreement with the collected porewater data (Figure 2b and Figure 4d).

In contrast to SO_4 , the Ca and Na concentration and rate profiles are not noticeably affected by ion pairing due to their concentrations being substantially higher (Figure 2). Mg concentrations are in the same order as SO_4 and here MgSO_4° markedly reduces free Mg concentrations (Figure 4e). Nevertheless, there is only a minimal influence of the MgSO_4° ion pair on the diffusive transport resulting in a slight enrichment at about 50 cm.b.s.f.

Non-ideal effects on gypsum/anhydrite solubility

The potential effects of changing salinity, as well as temperature and pressure regimes will be demonstrated using the example of gypsum and by association anhydrite, which are by far the dominant sulfate minerals at the MMV. The modelled responses in solubilities are depicted in Figure 5 and are expressed as the total Ca and SO_4 concentration product in equilibrium with gypsum or anhydrite, also referred to as the stoichiometric equilibrium constant (K^*). As predicted from numerous experimental studies (e.g. Blount and Dickson, 1973; Bock, 1961; Hardie, 1967), gypsum solubility increases with increasing temperature, especially in strong electrolyte solutions. In contrast, anhydrite experiences a pronounced decrease in solubility with rising temperatures, particularly at seawater salinity. The transition between the two minerals is also strongly temperature-dependent and occurs around 50 °C in pure water and seawater and can be as low as 22 °C for halite-saturated solutions, with gypsum being more stable in the lower temperature range. Increasing pressure raises both gypsum and anhydrite solubility because the sum of the aqueous molar volumes of the solute species is smaller than the molar volume of the minerals and water. While the effect appears to be less dramatic compared to the temperature influence, for anhydrite solubility in pure water a pressure increase of several hundred bar outweighs the effect of a temperature increase of about 50 °C.

Salinity appears to exert by far the strongest influence on $\text{CaSO}_4(\text{s})$ solubility. Adding about 2 mol kg^{-1} NaCl to seawater/pure water increases the gypsum stoichiometric equilibrium constant by over an order of magnitude (Figure 5c). Above 3 mol kg^{-1} added NaCl the trend reverses, albeit less markedly and the trend continues when the transition to anhydrite takes place at about 5 mol kg^{-1} added NaCl.

The strong sensitivity of the $\text{CaSO}_4(\text{s})$ solubility to changing pTS conditions is in part related to the formation of the CaSO_4° ion pair, however, deviation in the activity coefficients, activity of water and thermodynamic equilibrium constants seem to outweigh the influence of the ion pairing, especially at high salinities and temperatures. For example, the activity coefficient of SO_4 in halite saturation solutions is being reduced to 20% and that of Ca is being increased by almost an order of magnitude compared to the seawater value.

The potentially strong difference in the activity coefficients of SO_4 and Ca raises another often overlooked issue: Stoichiometric solubility products (K^*) are usually derived for symmetric stoichiometric solutions. In the presence of other electrolytes, such as NaCl, the stoichiometric K^* changes, due to the differing effects of the additional ions on the activity coefficients and the effect is well documented (e.g. Hofmann et al., 2010; Millero, 1995; Roy et al., 1993). Little is known, however, about the effect that is exerted on K^* by dominant electrolytes introducing one of the ions in great excess (i.e. CaCl_2 or Na_2SO_4). Figure 5d shows that with increasing concentration of the common ion electrolyte, K^* also increases, which is especially pronounced when Ca or SO_4 are present at $x_i < 0.2$ (representative of the presence of, for example, CaCl_2 or Na_2SO_4 in excess of $0.07 \text{ mol kg}_{\text{H}_2\text{O}}^{-1}$). In the rising MMV fluids, Ca and SO_4 are present at very different concentrations (e.g. 100 and 20 mmol kg^{-1} , respectively), making it necessary to include the effect of non-stoichiometric Ca/ SO_4 ratios on the $\text{CaSO}_4(\text{s})$ solubility. Figure 6 shows that the effect is however comparatively small and is only noticeable as a slight increase in solubility at the lower end of the mixing zone where the influence of the low SO_4/Ca ratios (i.e. 0.18) in the rising MMV fluids is strongest. It is mainly the strong NaCl gradient in the mixing zone that induces considerable fluctuations in the gypsum solubility (Figure 6), with the solubility almost doubling downcore.

Sulfate mineral precipitation in MMV fluids

Shallow MMV sediments contain several wt% of sulfur, which is attributed to the presence of ubiquitous gypsum microcrystals (Haffert et al., 2013). From the radiogenic strontium isotopic signal we know that these crystals have precipitated authigenically close to the seafloor, probably within the seawater mixing zone. As indicated by the saturation states in the lowermost porewater samples (Figure 2j-l), rising MMV fluids are saturated with respect to gypsum, barite and celestite. Similar trends for all three minerals can be observed throughout the mixing zone of the Bubble site: A zone of supersaturation is present at about 1 – 2 m.b.s.f. and while at first sight one might link this occurrence to the observed SO_4 peak, it is in fact the SO_4 activity, not the concentration, which contributes to the gypsum saturation. The concentration peak is only a side effect of the strong salinity gradient in the seawater mixing zone (as discussed above) and is located slightly closer to the seafloor than the gypsum saturation peak (Figure 2). This suggests that the saturation peak is created by transport processes in the mixing zone rather than diagenetic processes, which could be confirmed by our transport-only model (Figure 2). The modelled profiles successfully simulate the peak in supersaturation for gypsum and celestite. In the case of barite, the poor Ba modelling fit results in a marked underestimation of the peak.

Assuming that the extent of supersaturation at the Bubble site is sufficient to induce gypsum precipitation, a transport-reaction model was set up to quantify the amount of gypsum potentially precipitating in the shallow sediments as a result of this phenomenon (Table 5). Weak oversaturation and limited resupply of the dissolved constituents appear to significantly limit this process so that at it would take at least 10,000 years, even longer at

precipitation rates of less than 10 mM a^{-1} to produce the observed amount of several wt% gypsum in the MMV sediment.

Interestingly, this particular process of supersaturation cannot be found at any other site at the MMV due to its sensitivity to the upward fluid advection rate; In the case of the more distal sites (West and East) the advective flux of Ca is too weak, i.e. the diffusive flux is the dominant transport process. And in the case of the central Top site, the advective flux is too strong, limiting SO_4 diffusion into the sediment and thereby inhibiting gypsum supersaturation. With the strong temperature dependence of the gypsum/anhydrite solubility in mind, modelling efforts were also focused on volcanic-related processes. The results have given insight into two temperature related scenarios that could contribute to the precipitation of authigenic gypsum in the MMV sediments:

- (i) Fluids leaching a $\text{CaSO}_4(\text{s})$ containing diapir become saturated with respect to gypsum or anhydrite at the pTS conditions prevailing around the diapir. Supersaturation of the fluids as a result of upward migration of saturated CaSO_4 fluids along a decreasing temperature and thus solubility gradient would result in authigenic gypsum precipitation even during dormancy where fluid flow is limited. A simple box model designed to estimate gypsum build up from this process predicts that during dormant times the build-up of several wt% of gypsum would take more than 10,000 years thus making this an inefficient process. During active times however, 10 to 100 years of high fluid and heat flow could suffice to produce the observed sediment sulfur content at the MMV (Table 5)
- (ii) Increased temperatures during an active mud volcano phase result in increased solubility and thus $\text{CaSO}_4(\text{s})$ dissolution. During the transition to dormant conditions cooling of the fluids, with heat dissipating 2-3 orders of magnitude faster than solute concentrations (Haffert et al., 2013), can also result in ubiquitous supersaturation. This was found to be efficient at producing the observed amount of gypsum in the upper metres of the sediment after approximately 100 cycles. There is only a temperature difference of around 10°C between the gypsum-anhydrite transition temperature (22°C) and the bottom water temperature (ca. 12°C) yielding merely 0.03 wt% of sulfur per cycle. Thus, only a slight increase in the mud volcano activity, raising the temperature by $5\text{--}10^\circ\text{C}$, would be necessary per cycle (Table 5).

Discussion

Species coupling – implications

The MMV porewater profiles provide an excellent opportunity to highlight and quantify the importance of the non-ideal effects on the transport of solutes. At first sight it would appear that solutes such as Ba, K, Mg and SO_4 , whose profiles significantly deviate from a simple seawater mixing line (Figure 2a-i), must be involved in shallow ($< 200 \text{ cm.b.s.f.}$) diagenetic reactions (Haffert et al., 2013). However, based on a Na-Ca-Cl- SO_4 - H_2O Pitzer model, Haffert et al. (2013) concluded that at least the SO_4 profile peak likely results from the strong Na and Cl concentration gradient, and suggested the corresponding change in all ionic activity coefficients as the main cause.

The transport-reaction model of this study confirms that the solute profiles are strongly shaped by non-ideal effects arising from the steep NaCl gradient and much better agreement with the observed data for all modelled ions could be achieved (Figure 2a-i).

The noticeable effect of species coupling in extreme diagenetic settings has remained largely unstudied so far. The only study known to the authors that addresses species redistribution through similar transport processes, is the one by Felmy and Weare (1991). They investigate the process of diffusion along a salinity gradient created by a hypothetical salt dome in a theoretical case study. Their model predicted, similar to the findings at the MMV, that right at the onset of a salinity gradient, Ca and Mg become depleted while SO_4 accumulated. Their reasoning is slightly different from this study as they use Onsager diffusion coefficients for all their species and base their discussion largely on species coupling through off-diagonal diffusion. Because field data was absent in this case study, the model predictions could not be confirmed, however. While experimental setup have indeed provided valuable insight into diffusion along high-concentration gradients (e.g. Carey et al., 1995), here we show one of the first examples where the redistribution of species concentrations due to species coupling effects can be observed in a natural setting. Moreover, the presented model proved to be essential in the interpretation of the porewater data; ignoring these non-ideal effects in the presence of a significant salinity (or temperature) gradient has potentially far-reaching implications for the interpretation of collected data. For example, species redistribution may be credited to reactive processes and seafloor flux calculations may be grossly erroneous. The correct simulation of SO_4 is in many studies of particular importance as it is used to derive AOM rates and SO_4 derived CH_4 fluxes, the latter being the only way to reliably calculate the upward flux of dissolved CH_4 at seep sites.

The extent to which the non-ideal transport phenomena influence the species profile can be visualised as deviations from the simplified Fick model (Figure 2a-i). Generally, non-ideal effects are strongest where spatial changes in the activity coefficient and electrostatic field are most pronounced. This is especially true for SO_4 , which is particularly sensitive to the salinity and electrostatic gradient. The resultant transport-driven SO_4 concentration peak is an astounding outcome because here the chemical potential gradient at the seawater-sediment interface is decreasing while the concentration gradient is increasing. This illustrates that non-ideal effects in a natural setting can create a situation where a solute diffuses along its increasing (!) concentration gradient (Figure 2b and Figure 4b).

While the concept of using activities in reaction equilibria is well established, their application in transport models requires some further consideration. Activities represent the free fraction of a solute, corrected for non-ideal behaviour such as the tendency to form ion pairs. The transport forces calculated based on these activities are therefore valid only for the free concentration profile. When applying activity based transport forces on a total (i.e. combined free and ion pair) concentration it is assumed that the same transport forces that are valid for the free ion are also valid for the ion pair. This can introduce large errors to the model, as ion pairs have very different transport properties, i.e. they differ from their respective unassociated ions in their activity coefficients, valencies and sizes. In the case of the SO_4 simulation the profile was greatly improved when ion pairs were included as separately transported species.

Sulfate mineral paragenesis

The MMV has provided an excellent opportunity to broaden our understanding of gypsum and anhydrite paragenesis outside its usually evaporitic host environment. Here, the geochemical signal of an underlying salt diapir in conjunction with volcanic activity creates a setting where gypsum ubiquitously precipitates throughout the shallow marine sediment.

The fact that the overall morphology of gypsum was found to be rather variable (i.e. microcrystals, euhedral cm-scale minerals, fist-sized concretions also containing anhydrite) and the fact that the strontium isotopic ($^{87}\text{Sr}/^{86}\text{Sr}$) signal exhibited varying gradients within the crystals/concretions (Haffert et al., 2013) suggests that the paragenesis of authigenic gypsum/anhydrite is likely a combination of different precipitation processes. With the improved modelling of this study these processes could be further constrained providing better insight into the complicated dynamics of gypsum paragenesis and a semi-schematic diagram interpreting the related processes is provided in Figure 7. During **dormant** times inefficient gypsum precipitation occurs from saturated porewater rising along the weak geothermal gradient. During times when fluid velocities prevail at several cm per year, localised gypsum supersaturation can also occur as a result of non-ideal transport effects in the seawater mixing zone. This is the first time that this process has been documented but it was found to also be an inefficient process that can not generate the observed sediment sulfur content of several wt% at the MMV. With an increase in volcanic activity, an initial fluid pulse travels upwards preceded by a heat pulse due to the faster dissipation of heat. Above the gypsum-anhydrite transition zone, this heat pulse will cause some initial dissolution of gypsum, followed by flushing with gypsum saturated fluids.

During **active** times, increased temperatures shift the gypsum-anhydrite boundary significantly closer to the seafloor (up to within metres) which is accompanied by high fluid flow or even mud flow. The latter, efficiently transports gypsum or anhydrite crystals into the sediment column above the diapir, some of which is released into the porewater during their ascent as temperatures fall and anhydrite becomes more soluble (Figure 5a). When these Ca - and SO_4 - enriched fluids meet the mixing zone near the seafloor, where temperatures exhibit a strongly decreasing gradient accompanied by decreasing gypsum solubility, strong gypsum supersaturation results.

When the mud volcano activity subsides, the cooling of these gypsum-saturated fluids causes widespread supersaturation of gypsum. Repetitive changes in volcanic activity resulting in local temperature changes of at least 5-10 °C in the shallow sediment proved also to be an efficient process for accumulating authigenic gypsum in the sediment.

Conclusions

This work demonstrates that integrating the salinity gradient and resultant species coupling into the transport model results in an entirely different interpretation of the porewater profiles observed at the MMV (and potentially also other seeps with strong changes in salinity). Strong coupling between the dominant Na and Cl ions with the remaining solutes created porewater profile shapes at the MMV that differ profoundly from a typical seawater mixing zone. Furthermore, in the case of SO_4 , the simulation was significantly improved by acknowledging the formation of ion pairs. The good agreement between the modelled and observed profiles allowed, for the first time, verification of these theoretical transport phenomena in the field.

Correct diffusive transport calculations are critical to the interpretation of a number of processes, for example: (i) constraining fluid flow velocities, an essential aspect of diagenetic modelling of seeps, can be substantially flawed when neglecting non-ideal transport phenomena. At the MMV the error surpassed 50%. (ii) Reactive fluxes, which are usually indicated by deviations from the Fickian mixing profile, can be profoundly misjudged. Pronounced species enrichment and depletion at the MMV are in fact mainly transport-controlled. (iii) Flux calculations at the sediment-

seawater interface, an important means to evaluate the chemical exchange between both Earth reservoirs, can vary greatly between the simplified Fickian model and the non-ideal diffusion model. The SO_4 model results at the MMV are especially intriguing in that SO_4 diffuses along its increasing concentration gradient. In other words, the predicted diffusional fluxes at the seawater-sediment interface are of opposite direction to that which would be expected from the observed concentration profile.

With the help of the presented diagenetic model, the understanding of the sulfate mineral paragenesis at the MMV could be greatly advanced. Rising MMV fluids are saturated not only with respect to halite but also with respect to the minerals gypsum, barite and celestite. Because authigenic gypsum crystals were ubiquitously found in the MMV sediment cores and the fact that barite and celestite have significantly lower solubilities than gypsum, sulfate mineral paragenesis was investigated primarily on the example of gypsum. The solubility of gypsum, in particular its sensitivity to changes in pTS, were quantified and related to the present day MMV mixing zone: Thermodynamic modelling has shown that strong gradients in NaCl concentration and the small SO_4/Ca ratio (i.e. strong common ion effect) induce pronounced thermodynamic fluctuations with the gypsum solubility almost doubling in the seawater mixing zone.

Based on the improved understanding of gypsum solubility, different processes creating supersaturation with respect to gypsum were derived and quantified with respect to the MMV gypsum sediment content. Porewater data show a zone of gypsum supersaturation at about 1 – 2 m.b.s.f and our coupled thermodynamic transport-reaction model TRACTION relates this peak to a newly found transport-induced process. Here, downward-diffusing seawater-derived SO_4 ions encounter strongly Ca-enriched rising fluids, where rising fluids are saturated with respect to halite and gypsum and contain SO_4 concentrations significantly lower than in seawater. This unique process is very sensitive to the fluid advection rate and the fact that it can only account for very slow build-up of gypsum suggests that it plays only a minor role in the build-up of authigenic gypsum at the dynamic MMV.

Temperature-related scenarios have proven to be far more efficient to build up gypsum. These make use of the temperature control on gypsum solubility, i.e. gypsum solubility increases with increasing temperature, especially in strong electrolyte solutions, and the inherently transient nature of mud volcanoes. Especially during active times when rising mud and fluids cool along a strong temperature gradient, efficient precipitation of gypsum is possible. Repetitive cooling as part of volcanic activity cycling could also play a major role in the gypsum paragenesis, even if temperatures fluctuate only by 5 – 10 °C. The fact that the authigenic gypsum morphologies at the MMV are rather variable suggests that they have been created by a combination of the above described processes.

To conclude, modelling of the MMV fluids has highlighted the importance of accurate solubility modelling in extreme environmental settings deviating from standard thermodynamic conditions. Changes in activity coefficients, activity of water, thermodynamic equilibrium constants, ion pair concentrations and concentration ratios, exert a complex control on transport processes and on sulfate mineral geochemistry. Simplified approaches, such as the use of the Fickian diffusion model or generic stoichiometric equilibrium constants, can only account for some of the effects and can potentially generate significant errors when applied outside their validity range.

Acknowledgements

The authors gratefully acknowledge the constructive comments from four anonymous reviewers.

ACCEPTED MANUSCRIPT

Figure captions

Figure 1: Location map of the sampling stations at the Mercator mud volcano in the Gulf of Cadiz (cruise MSM1/3). Seafloor depth contours (metres below sea level) at the Mercator MV are in 20 m increments. This study focuses on the porewater profiles retrieved at the Bubble site.

Figure 2. a-i) Concentration - depth profiles of modelled solute species at the Bubble site of the MMV showing (i) analytical data (blue circles), (ii) profiles of the Onsager model (transport-only with the exception of ion pair reactions, black line) (iii) profiles of the Fickian model (grey line) and (iv) species activities (grey broken line). **j-l)** Saturation state (Ω) of gypsum, barite and celestite in analytical and modelled porewater (Bubble site). The porewater is saturated with respect to the mineral if the value for Ω takes on a value of 1, as indicated in the diagram. **m)** Solute activities of the species involved in the formation of sulfate minerals including arrows indicating the diffusion direction. Corresponding model parameters and terms are presented in Table 1 and Table 2.

Figure 3. Details of the model environment at the seawater-sediment mixing zone of MMV Bubble site. **a)** Porosity **b)** Activity of water and solution density (in g/cm^3), **c)** Electrostatic field contributing to ionic diffusion **d)** Total solution charge when including the effects of the electrostatic gradient (Onsager model, black) and when ignoring electrostatic effects (Fickian model, grey). **e)** Change in fluid velocity with depth

Figure 4. a,b) Visualisation of the effect that the spatial change of the activity coefficient has on the diffusion of SO_4 at the Bubble site, including the SO_4 excess chemical potential (μ_{ex}) (a) and the profile of the natural logarithm of the SO_4 activity, which is the sum of the natural logarithm of the SO_4 molality and activity coefficient (b). With the activity coefficient controlled by the overall change in the solutions composition, most importantly the NaCl gradient, the SO_4 concentration profile is shaped by the equilibrium fluxes driven by the excess chemical potential ($\mu_{ex} = RT \ln a_i$). Here, the extreme reduction of the SO_4 activity coefficient with depth is compensated by the localised increase in the SO_4 concentration. **c-g)** Effect of the formation of ion pairs on SO_4 diffusion, including concentration profiles of the major sulfate ion pairs (c), a comparison of the Onsager model transporting ion pairs (black) and the model neglecting ion pairs (grey) for SO_4 (d) and Mg (e) with $t\text{SO}_4 = \text{free } \text{SO}_4 + \text{NaSO}_4^- + \text{CaSO}_4^0 + \text{MgSO}_4^0$. The effect of ion pairs on the overall transport rates for SO_4 are shown in (f) including the total diffusion rates (combined chemical and electrostatic contributions, solid line) and advective rates (broken line). Note, the total reactive rate amounts to zero. Details on all the rates shaping the SO_4 profile are shown in (g) including diffusive (green), advective (red), and reactive (via ion pairing, purple) rate contributions. Diffusive rate contribution from the chemical ('chem', light green) and electrical ('electr', dark green) potential gradients are shown separately.

Figure 5. Gypsum (blue) and anhydrite (red) solubility in pure water (solid line), seawater (dashed line) and halite saturated (dotted line) solutions in changing environmental conditions including: **a)** Temperature, **b)** Pressure, **c)** NaCl (in addition to existing NaCl) and **d)** molar fraction of SO_4 (x_{SO_4}) with respect to the combined Ca- SO_4 content. For simplicity and ease of comparison, two NaCl dominated systems (seawater and halite saturated solution) were chosen so that activity coefficients are largely determined by Na and Cl related Pitzer parameters and the theoretical

addition of minor common ion electrolytes would change only the SO_4 and Ca ratio and not noticeably their activity. If not otherwise stated standard conditions are applied (25 °C and 1 bar). Solubility is expressed as the stoichiometric equilibrium constant K^* ($\text{mol}^2/\text{kg}_{\text{H}_2\text{O}}^2$) and is valid for total solute concentrations (disregarding ion pairs). Black arrows indicate the gypsum-anhydrite transition point, where applicable. For clarity only the thermodynamically stable $\text{CaSO}_4(\text{s})$ phase is shown. The Christov and Moller (2004a; 2004b) dataset (general Pitzer coefficients) and the Krumgalz et al. (2000) dataset (volumetric Pitzer coefficients) were used for temperature and pressure corrected equilibrium calculations. Note that temperature parameterisations were not used outside their validity range due to the strong divergence of the Na- SO_4 Pitzer parameters below its lower temperature limit of 25 °C.

Figure 6. 3-D representation (coloured surface) of gypsum solubility (expressed as the stoichiometric equilibrium constant (K_{Gypsum}^*) with increasing NaCl concentration and changing SO_4 molar fraction ($x_{\text{SO}_4} = \frac{m_{\text{SO}_4}}{m_{\text{SO}_4} + m_{\text{Ca}}}$) at 12 °C. When dissolved in pure water $x_{\text{SO}_4} = 0.5$, but in the presence of salts containing Ca or SO_4 this ratio changes (common ion effect). The MMV mixing zone is characterised by strong changes in the solutions composition, including NaCl concentration and x_{SO_4} resulting in drastic gradients in gypsum solubility (black line).

Figure 7. Modelled gypsum-anhydrite phase transition (red line) versus varying geothermal gradients. A conceptual presentation of the gypsum (Gy) and anhydrite (An) paragenesis in the context of volcanic activity cycling is added. Grey arrows represent precipitation (ppt) and dissolution (diss) processes related to transport along the geothermal gradient. Cycling between dormant and active MV states results in upward transport of diapiric $\text{CaSO}_4(\text{s})$ in porewater and sediment as well as the build-up of gypsum during cooling event. In the seawater mixing zone, diffusion-driven gypsum precipitation occurs at low fluid flow (Table 5). Note: the upper range of the geothermal gradient is only applicable to the top few metres of the mud volcano during active times.

References

- Bain, R.J. (1990) Diagenetic, nonevaporative origin for gypsum. *Geology* 18, 447-540.
- Ball, J.W. and Nordstrom, D.K. (1991) User's Manual for WATEQ4F, with Revised Thermodynamic Data Base and Test Cases for Calculating Speciation of Major, Trace, and Redox Elements in Natural Waters. US Geological Survey / Open-File Report.
- Berner, R.A. (1980) Early Diagenesis - A Theoretical Approach. Princeton University Press, Princeton, New Jersey.
- Blount, C.W. (1977) Barite solubilities and thermodynamic quantities up to 300 °C and 1400 bars. *American Mineralogist* 62, 942-957.
- Blount, C.W. and Dickson, F.W. (1973) Gypsum-Anhydrite Equilibria in Systems $\text{CaSO}_4\text{-H}_2\text{O}$ and $\text{CaCO}_3\text{-NaCl-H}_2\text{O}$. *American Mineralogist* 58, 323-331.
- Bock, E. (1961) On the solubility of anhydrous calcium sulphate and of gypsum in concentrated solutions of sodium chloride at 25 °C, 30 °C, 40 °C, and 50 °C. *Canadian Journal of Chemistry* 39.
- Boudreau, B.P. (1996) Diagenetic Models and Their Implementation: Modelling Transport and Reactions in Aquatic Sediments. Springer-Verlag, Berlin, Heidelberg, New York.
- Carey, A.E., Wheatcraft, S.W., Glass, R.J. and O'Rourke, J.P.-. (1995) Non-Fickian ionic diffusion across high-concentration gradients. *Water Resources Research* 31, 2213-2218.
- Christov, C. (2012) Temperature variable chemical model of bromide–sulfate solution interaction parameters and solid–liquid equilibria in the Na–K–Ca–Br– $\text{SO}_4\text{-H}_2\text{O}$ system. *Calphad* 36, 71-81.
- Christov, C. and Moller, N. (2004a) A chemical equilibrium model of solution behavior and solubility in the H–Na–K–Ca–OH–Cl– $\text{HSO}_4\text{-SO}_4\text{-H}_2\text{O}$ system to high concentration and temperature. *Geochimica et Cosmochimica Acta* 68, 3717-3739.
- Christov, C. and Moller, N. (2004b) Chemical equilibrium model of solution behavior and solubility in the H–Na–K–OH–Cl– $\text{HSO}_4\text{-SO}_4\text{-H}_2\text{O}$ system to high concentration and temperature. *Geochimica et Cosmochimica Acta* 68, 1309-1331.
- Debye, P. and Hückel, E. (1923) The theory of electrolytes. I. Lowering of freezing point and related phenomena. *Physikalische Zeitschrift* 24, 185-206.
- Felmy, A.R. and Weare, J.H. (1986) The prediction of borate mineral equilibria in natural waters: Application to Searles Lake, California. *Geochimica et Cosmochimica Acta* 50, 2771-2783.
- Felmy, A.R. and Weare, J.H. (1991) Calculation of multicomponent ionic diffusion from zero to high concentration: I. The system Na–K–Ca–Mg–Cl– $\text{SO}_4\text{-H}_2\text{O}$ at 25°C. *Geochimica et Cosmochimica Acta* 55, 113-131.
- Fick, A. (1855) Über Diffusion. *Annalen der Physik und Chemie* 94, 59-86.
- Greenberg, J.P. and Moller, N. (1989) The prediction of mineral solubilities in natural waters: A chemical equilibrium model for the Na–K–Ca–Cl– $\text{SO}_4\text{-H}_2\text{O}$ system to high concentration from 0 - 250°C. *Geochimica et Cosmochimica Acta* 53, 2503-2518.
- Haeckel, M., König, I., Riech, V., Weber, M. and Suess, E. (2001) Pore water profiles and numerical modelling of Peru Basin deep-sea sediments. *Deep-Sea Research II* 48, 3713-3736.
- Haffert, L. and Haeckel, M. (2018) TRACTION - a transport reaction model specifically designed to account for non-ideal transport and reaction effects. *PANGAEA* <https://doi.pangaea.de/10.1594/PANGAEA.894719>.
- Haffert, L., Haeckel, M., Liebetrau, V., Berndt, C., Hensen, C., Nuzzo, M., Reitz, A., Scholz, F., Schönfeld, J., Perez-Garcia, C. and Weise, S.M. (2013) Fluid evolution and authigenic mineral paragenesis related to salt diapirism – The Mercator mud volcano in the Gulf of Cadiz. *Geochimica et Cosmochimica Acta* 106, 261-286.
- Hardie, L.A. (1967) The gypsum-anhydrite equilibrium at one atmosphere pressure. *American Mineralogist* 52, 171-200.
- Harned, H.S. and Owen, B.B. (1958) The Physical Chemistry of Electrolyte Solutions. A.C.S. Monograph Reinhold Pub. Corp., London.
- Harvie, C.E., Moller, N. and Weare, J.H. (1984) The prediction of mineral solubilities in natural waters: The Na–K–Mg–Ca–H–Cl– $\text{SO}_4\text{-OH-HCO}_3\text{-CO}_3\text{-CO}_2\text{-H}_2\text{O}$ system to high ionic strengths at 25°C. *Geochimica et Cosmochimica Acta* 48, 723-751.
- Hensen, C., Nuzzo, M., Hornibrook, E., Pinheiro, L.M., Bock, B., Magalhaes, V.H. and Brückmann, W. (2007) Sources of mud volcano fluids in the Gulf of Cadiz - indications for hydrothermal imprint. *Geochimica et Cosmochimica Acta* 71, 1232-1248.
- Hoareau, G., Monnin, C. and Odonne, F. (2011) The stability of gypsum in marine sediments using the entire ODP/IODP porewater composition database. *Marine Geology* 279, 87-97.
- Hofmann, A.F., Soetaert, K., Middelburg, J.J. and Meysman, F. (2010) AquaEnv: An Aquatic Acid–Base Modelling Environment in R. *Aquatic Geochemistry* 16, 507-546.

- Katz, A. and Ben-Yaakov, S. (1980) Diffusion of Seawater Ions. Part II. The Role of Activity Coefficients and Ion Pairing. *Marine Chemistry* 8, 263-280.
- Krumgalz, B.S., Pogorelskii, R., Sokolov, A. and Pitzer, K.S. (2000) Volumetric Ion Interaction Parameters for Single-Solute Aqueous Electrolyte Solutions at Various Temperatures. *Journal of Physical and Chemical Reference Data* 29, 1123-1140.
- Krumgalz, B.S., Starinsky, A. and Pitzer, K.S. (1999) Ion-interaction approach: pressure effect on the solubility of some minerals in submarine brines and seawater. *Journal of Solution Chemistry* 28, 667-692.
- Lasaga, A.C. (1979) The treatment of multi-component diffusion and ion pairs in diagenetic fluxes. *American Journal of Science* 279, 324-346.
- Lasaga, A.C. (1981) Influence of diffusion coupling on diagenetic concentration profiles. *American Journal of Science* 281, 553-575.
- Lassin, A., Christov, C., Andre, L. and Azaroual, M. (2015) A thermodynamic model of aqueous electrolyte solution behavior and solid-liquid equilibrium in the Li-H-Na-K-Cl-OH-H₂O system to very high concentrations (40 molal) and from 0 to 250 °C. *American Journal of Science* 315, 204-256.
- Marcus, Y. and Hefter, G. (2006) Ion Pairing. *Chemical Reviews* 106, 4585-4621.
- Millero, F.J. (1995) Thermodynamics of the carbon dioxide system in the oceans. *Geochimica et Cosmochimica Acta* 59, 661-677.
- Millero, F.J. and Schreiber, D.R. (1982) Use of the ion pairing model to estimate activity coefficients of the ionic components of natural waters. *American Journal of Science* 282, 1508-1540.
- Møller, N. (1988) The prediction of mineral solubilities in natural waters: A chemical equilibrium model for the Na-Ca-Cl-SO₄-H₂O system, to high temperature and concentration. *Geochimica et Cosmochimica Acta* 52, 821-837.
- Monnin, C. (1999) A thermodynamic model for the solubility of barite and celestite in electrolyte solutions and seawater to 200°C and to 1 kbar. *Chemical Geology* 153, 187-209.
- Niemann, H., Duarte, J., Hensen, C., Omereg, E., Magalhaes, V.H., Elvert, M., Pinheiro, L.M., Kopf, A. and Boetius, A. (2006) Microbial methane turnover at mud volcanoes of the Gulf of Cadiz. *Geochimica et Cosmochimica Acta* 70, 5336-5355.
- Onsager, L. (1931) Reciprocal Relations in Irreversible Processes. II. *Physical Review* 38, 2265-2279.
- Onsager, L. and Fuoss, R.M. (1932) Irreversible Processes in Electrolytes. Diffusion, Conductance, and Viscous Flow in Arbitrary Mixtures of Strong Electrolytes. *Physical Chemistry* 36, 2689-2778.
- Pirlet, H., Wehrmann, L.M., Brunner, B., Franks, N., Dewanckele, J., Van Rooij, D., Foubert, A., Swennen, R., Naudts, L., Boone, M., Cnudde, V. and Henriët, J.P. (2010) Diagenetic formation of gypsum and dolomite in a cold-water coral mound in the Porcupine Seabight, off Ireland. *Sedimentology* 57, 786-805.
- Pitzer, K.S. (1973) Thermodynamics of Electrolytes. I. Theoretical Basis and General Equations. *Journal of Physical Chemistry* 77, 268-277.
- Pitzer, K.S. and Kim, J.J. (1974) Thermodynamics of electrolytes. IV. Activity and osmotic coefficients for mixed electrolytes. *Journal of the American Chemical Society* 96, 5701-5707.
- Pitzer, K.S. and Mayorga, G. (1973a) Thermodynamics of electrolytes. III. Activity and osmotic coefficients for 2–2 electrolytes. *Journal of Solution Chemistry* 7, 539-546.
- Pitzer, K.S. and Mayorga, G. (1973b) Thermodynamics of Electrolytes: II. Activity and Osmotic Coefficients for Strong Electrolytes with One or Both Ions Univalent. *Journal of Physical Chemistry* 77, 2300-2308.
- Reardon, E.J. and Armstrong, D.K. (1987) Celestite (SrSO₄(s)) solubility in water, seawater and NaCl solutions. *Geochimica et Cosmochimica Acta* 51, 63-72.
- Robinson, R.A. and Stokes, R.H. (1959) *Electrolyte solutions. The measurement and interpretation of conductance, chemical potential and diffusion in solutions of simple electrolytes*, 2nd edition. Butterworths, London.
- Roy, R.N., Roy, L.N., Vogel, K.M., Porter-Moore, C., Pearson, T., Good, C.E., Millero, F.J. and Campbell, D.M. (1993) The dissociation constants of carbonic acid in seawater at salinities 5 to 45 and temperatures 0 to 45 °C (see erratum: *Mar Chem* 52:183, 1996). *Marine Chemistry* 44, 249-267.
- Scholz, F., Hensen, C., Reitz, A., Romer, R.L., Liebetrau, V., Meixner, A., Weise, S.M. and Haeckel, M. (2009) Isotopic evidence (⁸⁷Sr/⁸⁶Sr, ^δLi) for alteration of the oceanic crust at deep-rooted mud volcanoes in the Gulf of Cadiz, NE Atlantic Ocean. *Geochimica et Cosmochimica Acta* 73, 5444-5459.
- Siesser, W.S. and Rogers, J. (1976) Authigenic pyrite and gypsum in South West African continental slope sediments. *Sedimentology* 23, 567-577.
- Sommer, S., Linke, P., Pfannkuche, O., Schleicher, T., Schneider von Deimling, J., Reitz, A., Haeckel, M., Flögel, S. and Hensen, C. (2009) Seabed methane emissions and the habitat of frenulate tubeworms on the Captain Arutyunov mud volcano (Gulf of Cadiz). *Marine Ecology Progress Series* 382, 69-86.
- Stumm, W. and Morgan, J.J. (1996) *Aquatic Chemistry*, third ed. John Wiley & Sons, New York.

- van Driesche, A.E.S., Stawski, T.M., Benning, L.G. and Kellermeier, M. (2017) Calcium sulfate precipitation throughout its phase diagram, in: van Driesche, A., Kellermeier, M., Benning, L.G., Gebauer, D. (Eds.), New perspectives on mineral nucleation and growth - From solution precursors to solid materials. Springer, Switzerland, pp. 227-256.
- Wang, J.S., Suess, E. and Rickert, D. (2004) Authigenic gypsum found in gas hydrate-associated sediments from Hydrate Ridge, the eastern North Pacific. *Science in China Series D-Earth Sciences* 47, 280-288.
-

Figures

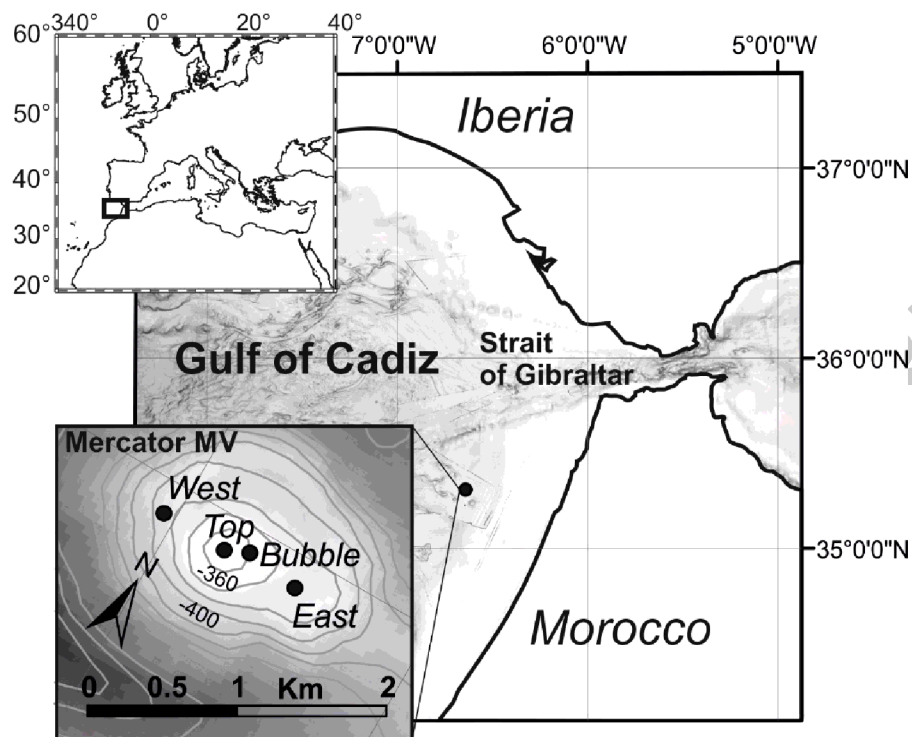


Figure 1

Solute profiles

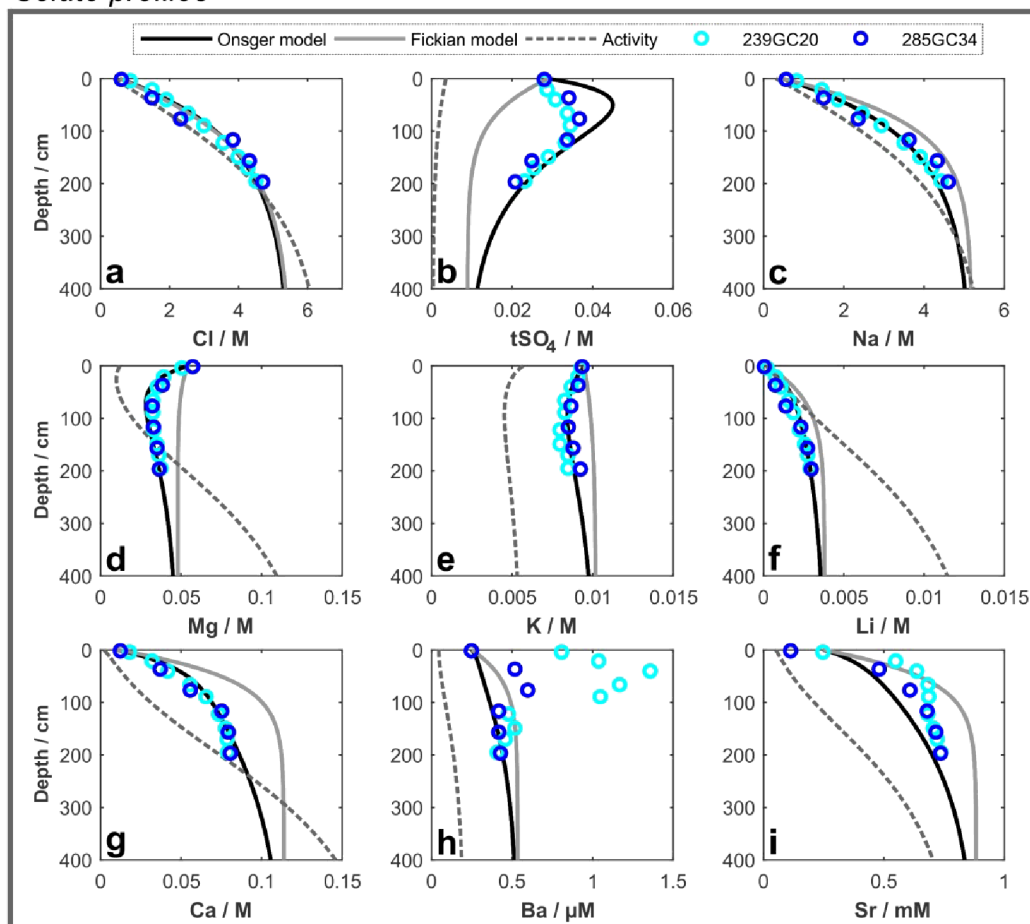


Figure 2

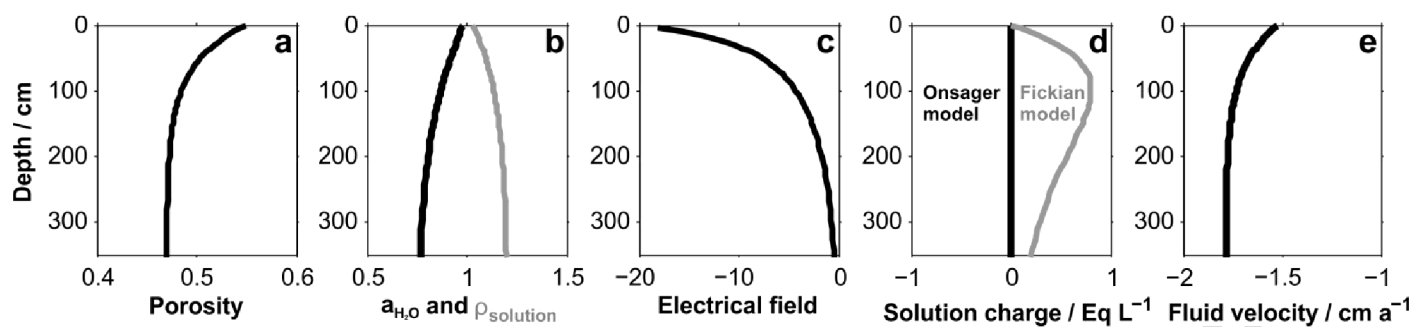
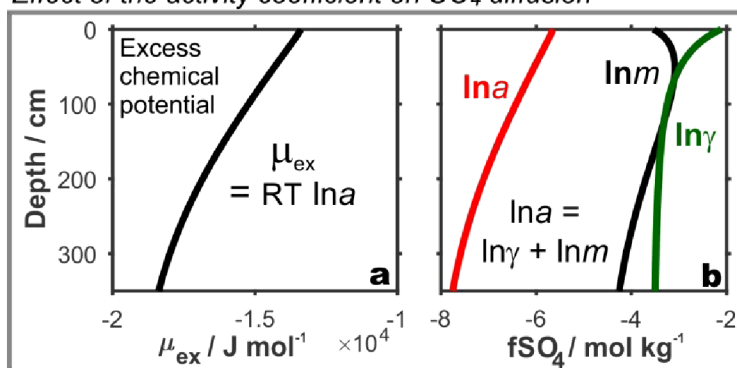


Figure 3

Effect of the activity coefficient on SO_4 diffusion



Effect of ion pairs on SO_4 diffusion

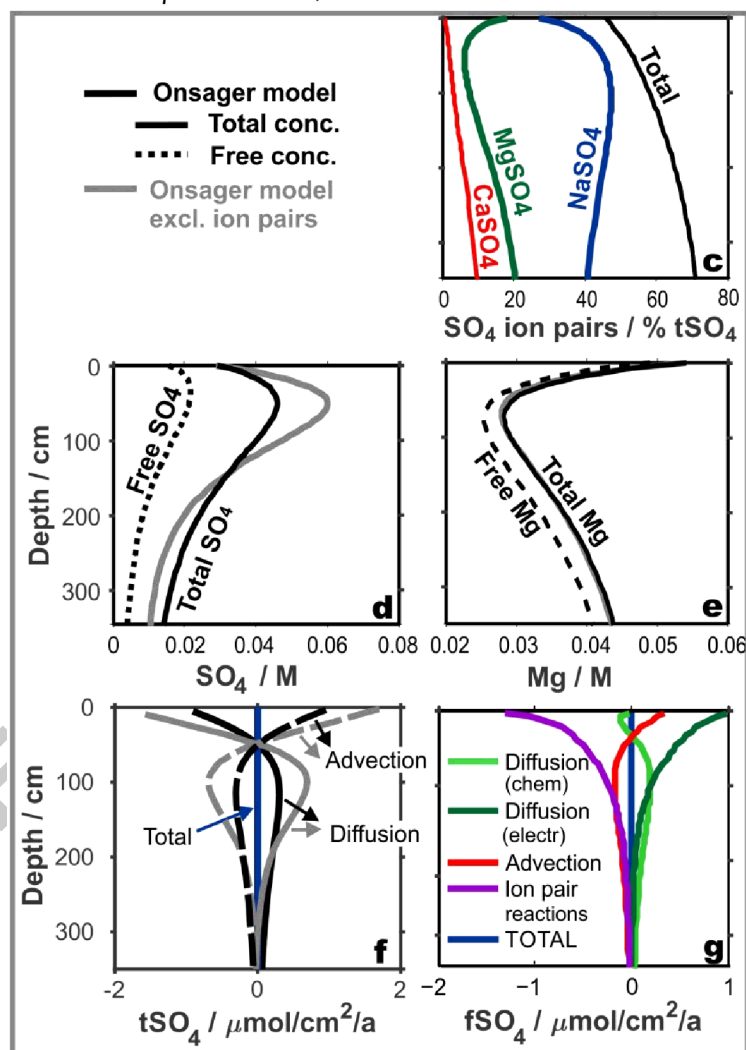


Figure 4

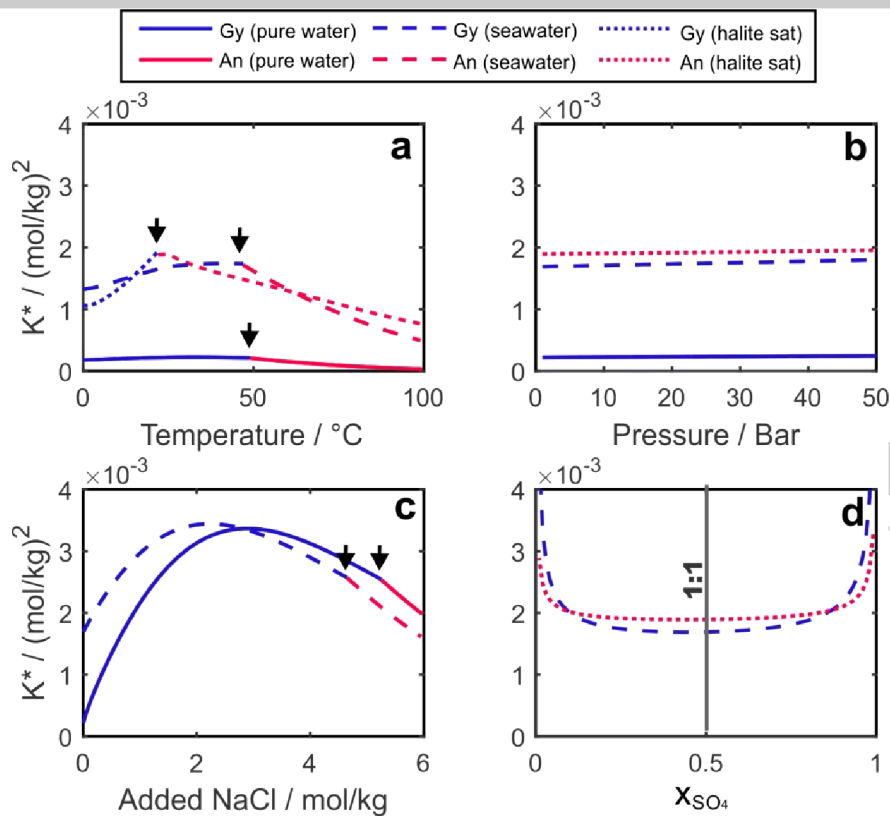


Figure 5

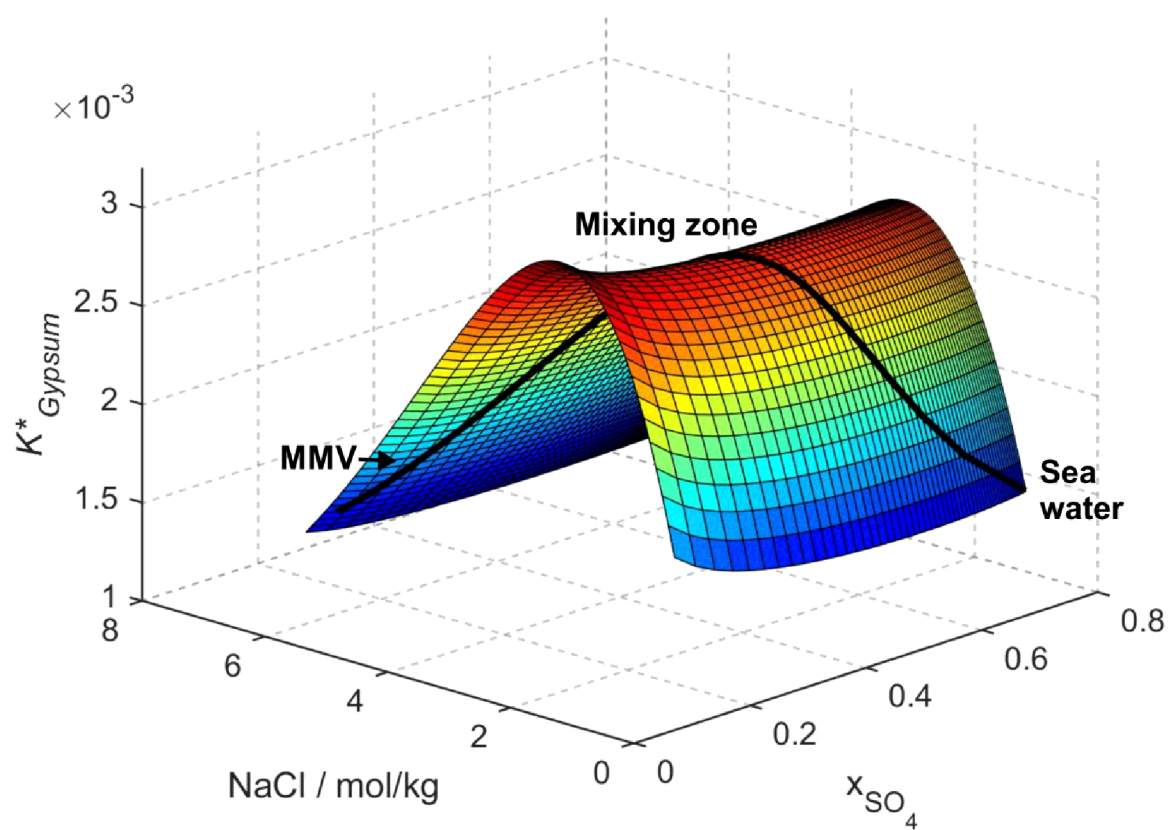


Figure 6

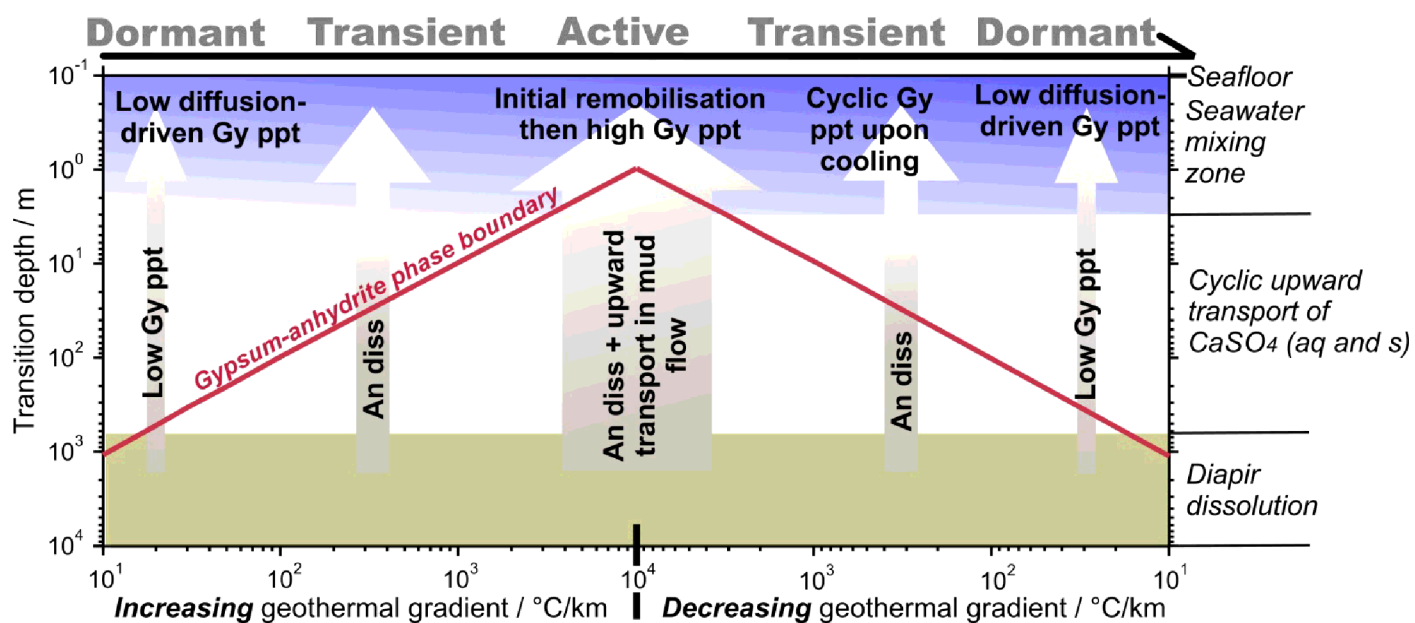


Figure 7

Tables

Table 1. Specifications of the Bubble site transport models (239GC20 and 285GC34)

<i>Model parameters</i>	<i>Specifier</i>	<i>Value</i>	<i>Unit</i>	
Time steps	t	1e6 (steady state)	a	
Maximum depth	L or x_{max}	800	cm	
Spatial grid points	n_x	76 (uneven spacing)		
<i>Environmental parameters</i>				
Geothermal gradient	dT/dx	30	°C km ⁻¹	
Pressure	P	3.7 - 4.5	Bar	
Temperature	T	12	°C	
Sedimentat burial rate (x = ∞)	w_{∞}	0.0001	cm _{BS} a ⁻¹	
Upward fluid velocity	v_0	1.5	cm _{PW} a ⁻¹	
Porosity at sediment surface (x=0)	ϕ_0	0.55		
Porosity at infinite depth (x = ∞)	ϕ_{∞}	0.47		
Porosity attenuation coefficient	β	0.017		
		<i>Tracer diffusion</i>		
<i>Species parameters</i>	<i>Upper (bw) boundary / mM</i>	<i>Lower boundary / mM</i>	<i>coefficient / cm² a⁻¹</i>	<i>Pitzer activity coefficient</i>
Na ⁺	478	5191 ^{1) 2)}	303.6 ³⁾	0.62 - 0.97
K ⁺	9.48	10.2	456.0 ³⁾	0.48 - 0.60
Ca ²⁺	10.4 ⁶⁾	114 ^{2) 6)}	181.3 ³⁾	0.20 - 1.42
Mg ²⁺	54.2 ⁶⁾	48.0 ⁶⁾	162.7 ³⁾	0.22 - 2.54
Li ⁺	0.243	3.80	230.9 ³⁾	0.69 - 3.15
Ba ²⁺	2.50E-04	5.34e-04 ²⁾	197.7 ³⁾	0.16 - 0.35
Sr ²⁺	0.248	0.883 ²⁾	180.4 ³⁾	0.20 - 0.84
Cl ⁻	558	5.51e+03 ¹⁾²⁾	468.6 ³⁾	0.67 - 1.07
SO ₄ ²⁻	28.9 ⁶⁾	8.90 ^{2) 6)}	241.7 ³⁾	0.03 - 0.12
NaSO ₄ ⁻	7.91 ⁵⁾	3.82 ⁵⁾	388.0 ⁴⁾	0.65 - 1.00 (= HSO ₄ ⁻)
CaSO ₄ [°]	0.204 ⁵⁾	1.13 ⁵⁾	268.1 (=MgSO ₄ [°])	unity
MgSO ₄ [°]	5.34 ⁵⁾	2.46 ⁵⁾	268.1 ⁴⁾	unity

1) Constrained by charge balance, **2)** set to halite, gypsum, celestite or barite saturation, respectively, **3)** Bourdreau (1996), **4)** Applin and Lasaga (1984), **5)** at equilibrium with the respective cation and anion, **6)** total (incl ion pairs) concentration

Table 2. Reaction parameters for mineral equilibria applied at the lower model boundary and for ion pair equilibria that are maintained throughout the model domain.

Species	Reaction	Saturation (Ω)/Equilibrium state (Eq)	Rate expression /mmol $a^{-1} L_{pw}^{-1}$	Equilibrium constant (log K)	Kinetic constant / a^{-1}
Gypsum	$C \ aO_2 \ 2H_2O = Ca^{2+} + SO_4^{2-} + 2H_2O$	$\Omega_{Gypsum} = \frac{a_{Ca^{2+}} \cdot a_{SO_4^{2-}} \cdot a_{H_2O}^2}{K_{Gypsum}}$	$R = k (\Omega - 1)$	-4.5195 ¹⁾	0.01 - 100
Anhydrite	$C \ aO_2 \rightleftharpoons Ca^{2+} + SO_4^{2-}$	$\Omega_{Anhydrite} = \frac{a_{Ca^{2+}} \cdot a_{SO_4^{2-}}}{K_{Anhydrite}}$	NA	-4.1389 ¹⁾	NA
Celestite	$Sr \ 2O_2 = Sr^{2+} + SO_4^{2-}$	$\Omega_{Celestite} = \frac{a_{Sr^{2+}} \cdot a_{SO_4^{2-}}}{K_{Celestite}}$	NA	-6.6171 ²⁾	NA
Barite	$B \ 2O_2 = Ba^{2+} + SO_4^{2-}$	$\Omega_{Barite} = \frac{a_{Ba^{2+}} \cdot a_{SO_4^{2-}}}{K_{Barite}}$	NA	-10.2195 ³⁾	NA
Halite	$N \ a \rightleftharpoons Na^+ + Cl^-$	$\Omega_{Halite} = \frac{a_{Na^+} \cdot a_{Cl^-}}{K_{Halite}}$	NA	1.5704 ⁴⁾	NA
CaSO ₄ [°]	$C \ aO_2 \rightleftharpoons Ca^{2+} + SO_4^{2-}$	$Eq_{CaSO_4^\circ} = \frac{a_{Ca^{2+}} \cdot a_{SO_4^{2-}}}{a_{H_2O}^2 \cdot K_{CaSO_4^\circ}}$	$R = k (\Omega - 1)$	-1.4335 ⁵⁾	0.1 ⁸⁾
MgSO ₄ [°]	$M \ gO_2 \rightleftharpoons Mg^{2+} + SO_4^{2-}$	$Eq_{MgSO_4^\circ} = \frac{a_{Mg^{2+}} \cdot a_{SO_4^{2-}}}{a_{H_2O}^2 \cdot K_{MgSO_4^\circ}}$	$R = k (\Omega - 1)$	-2.37 ⁶⁾	1000 ⁸⁾
NaSO ₄ ⁻	$N \ aO_2 \rightleftharpoons Na^+ + SO_4^{2-}$	$Eq_{NaSO_4^-} = \frac{a_{Na^+} \cdot a_{SO_4^{2-}}}{a_{H_2O}^2 \cdot K_{NaSO_4^-}}$	$R = k (\Omega - 1)$	0.9424 ⁷⁾	1000 ⁸⁾

1) Møller (1988) / Greenberg and Møller (1989), 2) Reardon and Armstrong (1987) / Monnin (1999), 3) Blount (1977) / Monnin (1999), 4) Harvie et al. (1984), 5) Møller (1988) / Greenberg and Møller (1989), 6) Stumm and Morgan (1996) / Ball and Nordstrom (1991), 7) Millero and Schreiber (1982), 8) arbitrarily set to maintain equilibrium

Table 3. Parameters through which species in the left column influence the Onsager transport model of the species in the upper row. These include Onsager coefficients (l), activity coefficients (γ), the electrical field (φ^E) and ion pair reactive equilibria (R). Differences between the sections above and below the grey diagonal arise from the fact that the electrical field and activities are calculated only from the major ion profiles.

	Na ⁺	K ⁺	Ca ²⁺	Mg ²⁺	Li ⁺	Ba ²⁺	Sr ²⁺	Cl ⁻	SO ₄ ²⁻	NaSO ₄ ⁻	CaSO ₄ [°]	MgSO ₄ [°]
Na ⁺	φ^E	γ, φ^E	γ, φ^E	γ, φ^E	γ, φ^E	γ, φ^E	γ, φ^E	γ, φ^E, l	$\gamma, \varphi^E, R_{NaSO_4}$	$\gamma, \varphi^E, R_{NaSO_4}$		
K ⁺	γ, φ^E	φ^E	γ, φ^E	γ, φ^E	γ, φ^E	γ, φ^E	γ, φ^E	γ, φ^E	γ, φ^E	γ, φ^E		
Ca ²⁺	γ, φ^E	γ, φ^E	φ^E	γ, φ^E	φ^E	φ^E	φ^E	γ, φ^E	$\gamma, \varphi^E, R_{CaSO_4}$	γ, φ^E	R_{CaSO_4}	
Mg ²⁺	γ, φ^E	γ, φ^E	γ, φ^E	φ^E	φ^E	φ^E	φ^E	γ, φ^E	$\gamma, \varphi^E, R_{MgSO_4}$	γ, φ^E		R_{MgSO_4}
Li ⁺												
Ba ²⁺												
Sr ²⁺												
Cl ⁻	γ, φ^E, l	γ, φ^E	γ, φ^E	γ, φ^E	γ, φ^E	γ, φ^E	γ, φ^E	φ^E	γ, φ^E	γ, φ^E		
SO ₄ ²⁻	$\gamma, \varphi^E, R_{NaSO_4}$	γ, φ^E	$\gamma, \varphi^E, R_{CaSO_4}$	$\gamma, \varphi^E, R_{MgSO_4}$	γ, φ^E	γ, φ^E	γ, φ^E	γ, φ^E	φ^E	$\gamma, \varphi^E, R_{NaSO_4}$	R_{CaSO_4}	R_{MgSO_4}
NaSO ₄ ⁻	R_{NaSO_4}								R_{NaSO_4}			
CaSO ₄ [°]			R_{CaSO_4}						R_{CaSO_4}			
MgSO ₄ [°]				R_{MgSO_4}					R_{MgSO_4}			

Table 4. Summary of non-ideal terms included in the presented models

Transport-only models		Transport-reaction model	
Onsager model ¹⁾		Fickian model	Onsager model ¹⁾
Total conc. model	Ion pair model		Ion pair model
$\frac{\partial a}{\partial x} = \frac{\partial \gamma m^T}{\partial x}$	$\frac{\partial a}{\partial x} = \frac{\partial \gamma m^F}{\partial x}$	$\frac{\partial a}{\partial x} = \frac{\partial C^T}{\partial x}$	$\frac{\partial a}{\partial x} = \frac{\partial \gamma m^F}{\partial x}$
$\frac{\partial \varphi^E}{\partial x} \neq 0$	$\frac{\partial \varphi^E}{\partial x} \neq 0$	$\frac{\partial \varphi^E}{\partial x} = 0$	$\frac{\partial \varphi^E}{\partial x} \neq 0$
$l_{ii} \neq l_{ii}^o$	$l_{ii} = l_{ii}^o = \frac{D_i^o C_i^F}{RT}$	$l_{ii} = l_{ii}^o = \frac{D_i^o C_i^T}{RT}$	$l_{ii} = l_{ii}^o = \frac{D_i^o C_i^F}{RT}$
$l_{ij} \neq 0$	$l_{ij} = 0$	$l_{ij} = 0$	$l_{ij} = 0$
$l_{ii}^{IP} = l_{ij}^{IP} = 0$	$l_{ii}^{IP} = \frac{D_i^o C_i^{IP}}{RT}; l_{ij}^{IP} = 0$	$l_{ii}^{IP} = l_{ij}^{IP} = 0$	$l_{ii}^{IP} = \frac{D_i^o C_i^{IP}}{RT}; l_{ij}^{IP} = 0$
$R_i = 0$	$R_{SO_4} = -R_{CaSO_4^\circ} - R_{MgSO_4^\circ} - R_{GyPPT}$ $R_{Ca} = -R_{CaSO_4^\circ}$ $R_{Mg} = -R_{MgSO_4^\circ}$	$R_i = 0$	$R_{SO_4} = -R_{CaSO_4^\circ} - R_{MgSO_4^\circ} - R_{GyPPT}$ $R_{Ca} = -R_{CaSO_4^\circ} - R_{GyPPT} + R_{GyDISS}$ $R_{Mg} = -R_{MgSO_4^\circ}$ $R_{Gy} = +R_{GyPPT} - R_{GyDISS}$

where a is the activity; C and m represent concentrations in molar and molal units, respectively; R defines the reactive contributions; the superscript ^T and ^F indicate total and free concentrations, respectively; γ is the molal-scale activity coefficient; l_{ij} and l_{ii} represent the off- and on-diagonal Onsager coefficients; The subscript ^{IP} is indicative of ion pairs and the superscript _{PPT} and _{DISS} represent precipitation and dissolution reactions, respectively. ¹⁾ In the absence of suitable Onsager coefficients, the following term is used instead: $l_{ii} = l_{ii}^o = \frac{D_i^o C_i^T}{RT}$

Table 5. Quantitative estimates of gypsum precipitation from three proposed mechanism driving gypsum saturated fluids towards supersaturation.

<i>1 – 5 wt% S sediment content (Bubble site)</i>	Fluid velocity / cm a⁻¹	Geothermal gradient / °C km⁻¹	Time interval / a	Volcanic cycles (dormant – active – dormant)
Shallow diffusion driven ppt	1.5	30	10 000	n.a.
Shallow temperature cycling (dormant-active)	n.a.	n.a.	n.a.	100
Asceding fluids – dormant conditions	1.5	30	10 000 000	n.a.
Asceding fluids/mud – active conditions	> 30	> 1000	1000	n.a.